Wide Field Optical Imaging on Hermes Fields: Observations and Source Catalogues

E. A. González-Solares et al.

ABSTRACT

We present U, g, r, i and Z band optical images and associated catalogues taken with the INT WFC on the FIRST Look Survey, ELAIS N1 and Lockman Hole fields. In this paper we outline the observations and data processing and characterize the completeness, reliability, photometric and astrometric accuracy of this dataset. All images have been photometrically calibrated using SDSS and compose a uniform and homogeneous dataset over all the observed fields. Magnitude limits are U, g, r, i, Z of 24.1, 24.9, 24.3, 23.6, 22.1 (AB, 5σ). **– Note: Only describing the FLS products at the moment –**

Key words: catalogs – surveys – galaxies:photometry

1 INTRODUCTION

This report describes mainly the INT WFC obtained in FLS and will be updated to incorporate all the data in EN1 and Lockman Hole. The main topics to include are:

- Description of observations and summary of data quality
- Data processing focusing in particular to astrometric and photometric calibration against SDSS.
- Description of catalogue contents and which magnitude to use in different cases. Also how to derive any aperture magnitude from the curve of growth.

Important. Catalogue magnitudes are now AB, calibrated against SDSS in the INT WFC system. If you want to compare stars in both systems then use the colour transformation provided in the text. Those do not have to be valid for comparison of galaxies though.

2 OBSERVATIONS

Observations have been made using the Wide Field Camera (WFC) on the 2.5m Isaac Newton Telescope (INT) on the Observatorio del Roque de Los Muchachos, La Palma. The INT WFC consists of four 2048x4096 pixel CCDs, covering a field of view of 0.29 sq. deg. with a pixel scale of 0.33 arcsec. The camera CCD detectors are configured in an L-shape and CCD number 3 is slightly vignetted in one corner. There is a small gap between detectors which leaves about 2% of the total field of view uncovered. In these observations we have not attempted to do offsets to cover the chip gaps. The broad-band filters are similar to the SDSS filters but slightly different resulting in the need to introduce colour equations to transform between both. In particular the WFC filters are slightly redder than their counterparts in SDSS as shown in figure 1 where the QE of the detector has also been taken into account.

In ELAIS N1 and Lockman Hole existing publicly available imaging data (by the Wide Field Survey and SWIRE) have been extended with newer data and all the existing data recalibrated to the same photometric reference producing homogenous data products over all the fields.

FLS images were obtained in four runs on semesters 01A, 05A, 05B, 06A and 09A. Images were acquired with one exposure of 600 seconds in each band. Weather conditions were variable across the different observing runs with both good photometric nights and some not so good ones. In particular U band frames were mostly obtained in bad seeing conditions having in mind existing deeper U band observations in the FLS which are incorporated to our catalogue. **– Note: This is still in process. –**

3 DATA PROCESSING

All the observations obtained with the INT telescope at La Palma are transmitted in pseudo-real time to the Cambridge Astronomy Survey Unit (CASU) for data archival via the internet. Although quasi real time data processing is possible it is preferable to perform the data processing on a run by run basis. The calibration is then performed using the whole run master flats and biases. For each observation the imaging data are stored in a Multi-Extension Fits file (MEF) with a primary header describing the overall characteristics of the observation (pointing, filter, exposure time, ...) and four image extensions corresponding to each of the CCD detectors.

The data are processed by CASU as described in Irwin and Lewis (2001) following the same steps as for the processing of the Wide Field Survey (Irwin et al. 2005; McMahon et al. 2001) which used the same telescope and camera combination. We provide here a short description of the reduction steps. **– Note: The description below is a bit too extensive and appears in other papers. Need to cut it down but leaving it for now for reference. –**

The data are first debiassed (full 2D bias removal is necessary). Bad pixels and columns are then flagged and recorded in

Table 1. Summary of observations and data quality

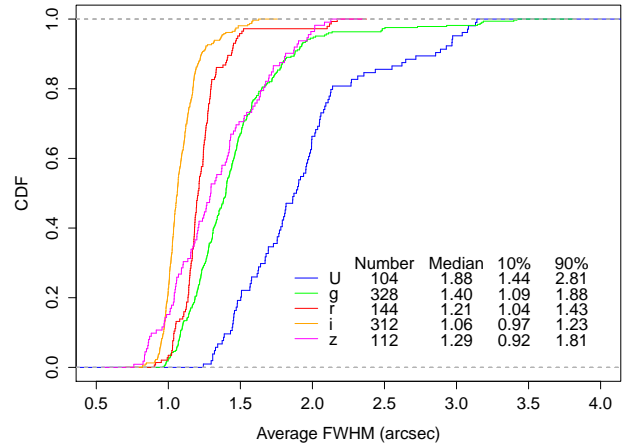|		First Look Survey			
Band	**Area (sq. deg.)**	**Median seeing (arcsec)**	**ZP[a]**	**ZP err**	**Depth (AB)[b]**
U_{WFC}		1.8 (1.4, 2.3)	23.63	0.03	24.1
g_{WFC}		1.4 (1.0, 1.8)	24.87	0.02	24.9
r_{WFC}		1.2 (1.0, 1.5)	24.67	0.02	24.3
i_{WFC}		1.0 (0.9, 1.6)	24.19	0.03	23.6
Z_{WFC}		1.3 (1.0, 2.1)	22.82	0.06	22.1
		ELAIS N1			
		Lockman Hole			

[a] Defined at unit airmass for a 1 sec exposure
[b] Magnitude limit is 5σ in a 1.2 arcsec radius
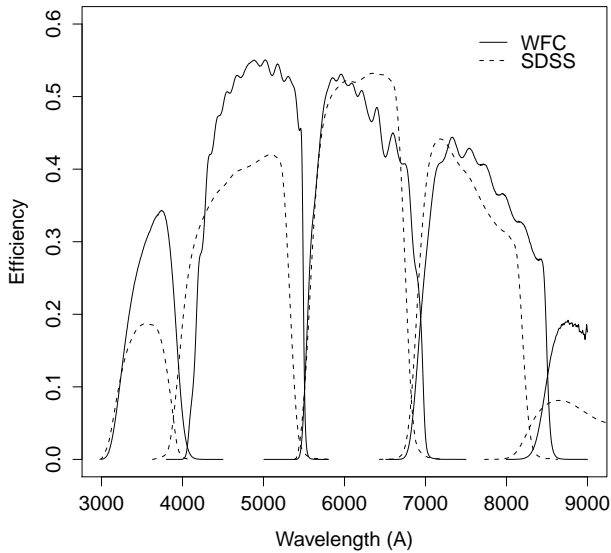
Figure 1. Efficiency curves of the UgriZ filters from the WFC (continuous line) and ugriz filters from SDSS (dashed line).

Figure 2. Seeing distribution.

confidence maps, which are used during catalogue generation. Linearity tests using sequences of dome flats revealed that the CCDs have significant non-linearities at the level of 1 to 2 per cent depending on the detector and period of observation. Due to several changes to the WFC controllers the linearity values change from time to time so linearity measurements are updated periodically. A linearity correction using look-up-tables is then applied to all data. Flatfield images in each band are constructed by combining a series of sky flats obtained in bright sky conditions during the twilight for each run.

We define a confidence c_{ij} map, where j refers to pixel j of frame i, that is an inverse variance weight map in units of relative variance denoting the confidence associated with the flux value in each pixel. The c_{ij} are normalised to a median level of 100 per cent (i.e. $\langle c_{ij} \rangle = 1$). This has the advantage that the same map can also be used to encode for hot, bad or dead pixels, by assigning zero confidence.

The confidence map for each frame is derived from analysis of the flat fields and is unique for each filter/detector combination.

It encodes individual pixel sensitivities and allows for vignetted or bad regions to be masked.

The standard catalogue generation software (Irwin 1985) makes direct use of the confidence maps previously generated for a variety of tasks. These include object detection and parametrization, producing quality control information, standard object descriptors and detected object overlay files. The possibly varying sky background is estimated automatically, prior to object detection, using a combination of robust iteratively clipped estimators. The image catalogues are then further processed to yield morphological classification for detected objects and used to generate astrometric and photometric calibration information.

Each detected object has an attached set of descriptors, forming the columns of the binary table and summarising derived position, shape and intensity information. During further processing stages ancillary information such as the sky properties, seeing and mean stellar image ellipticity, are derived from the catalogues and stored in the FITS headers attached to each catalogue extension. In addition to being the primary astronomical products from the pipeline processing, the catalogues and associated derived summary information form the basis for astrometric and photometric calibration and quality control monitoring.

Finally an astrometric solution starts with a rough World Coordinate System (WCS) based on the known telescope and cam-
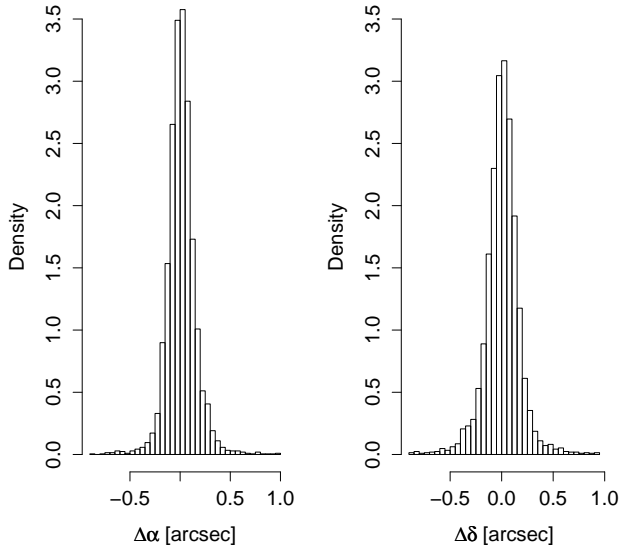
Figure 3. Differences in RA and Dec between the 2MASS positions and the derived WFC positions. The rms in these histograms is around 150 marcsec and it is dominated by the 2MASS rms errors.
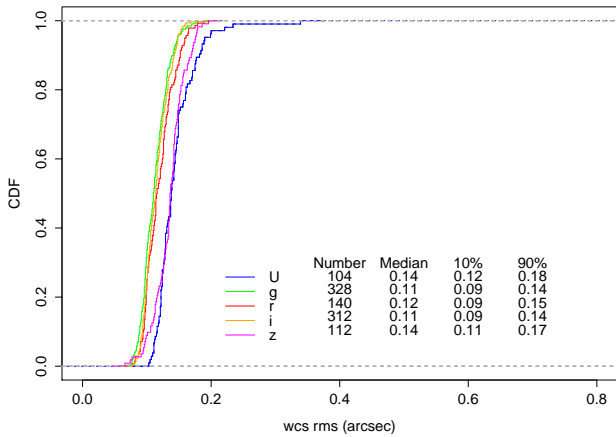

Figure 4. Cumulative density function showing the distribution of the astrometric residuals for each band in all chips; the median and the first and ninth deciles of the distribution are shown together with the number of chips.

era geometry and is then progressively refined using the 2MASS catalogue. The WFC field distortion is modelled using a zenithal equidistant projection with polynomial radial distortion (ZPN; Greisen and Calabretta 2002). The resulting internal astrometric precision is better than 100 mas over the whole WFC array (based on intercomparison of overlap regions).

The object detection is performed in each band separately using a standard APM-style object detection and parametrization algorithm (Irwin 1985). The curve-of-growth, defined as the flux inside an aperture as a function of its radius, is calculated measuring the flux in a set of 13 soft-edge apertures of radius $r/2$, $r/\sqrt{2}$, r, $\sqrt{2}r$, $2\sqrt{(2)}r$, $4r$, $5r$, $6r$, $7r$, $8r$, $10r$, $12r$ where $r = 3.5$ pixels (1.2 arcsec) and an automatic aperture correction (based on the av-
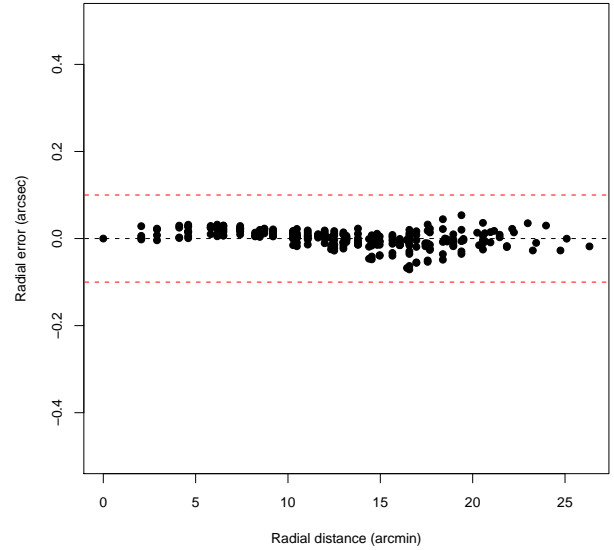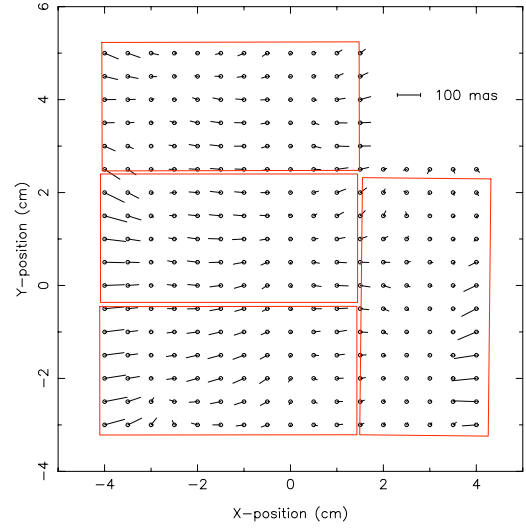

Figure 5. Top: Astrometric residuals derived from a series of independent WFC pointings. The residuals are shown in physical coordinates with respect to the center of the optical axis. Bottom: Radial error vs distance from stacking analysis of all frames.

erage curve-of-growth for stellar images) is applied to all detected objects. A soft-edged aperture divides the flux in pixels lying across the aperture boundary in proportion to the pixel area enclosed. All the apertures of selected isolated bright stars are used to determine the curve of growth.

Finally a distortion correction is applied to the photometry to take into account the change of scale with respect to the optical axis distance. The magnitude of the multiplicative correction to be applied to the measured flux can be modeled as (Irwin et al. 2009, in prep)

$$d = \left(1 + \frac{3\,P_3\,r^2 + 5\,P_5\,r^4}{P_1}\right)\left(1 + \frac{P_3\,r^2 + P_5\,r^4}{P_1}\right) \quad (1)$$

where R is the distance from the optical axis. We have remeasured the distortion coefficients for the recent WFC data and the coefficients are $P_1 = 1$, $P_3 = 210$ and $P_5 = 0$ except for the U
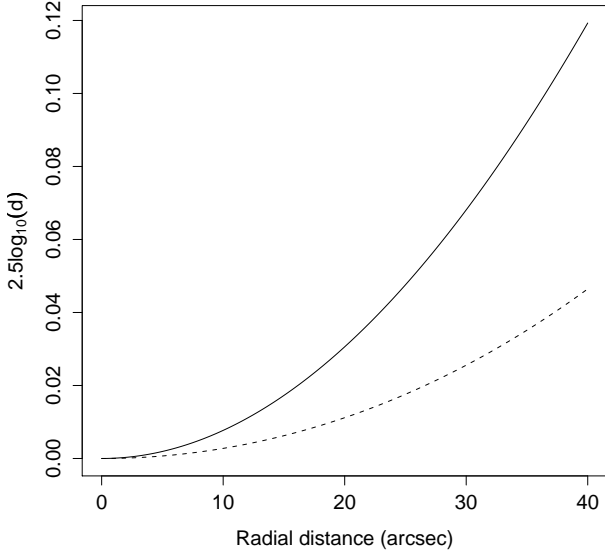
Figure 6. Effect of scale change in photometry (magnitude versus distance to field centre) for the WFC (continuous line) and MegaCam (dashed line).

band which is $P_3 = 80$ (corresponding to the `PV2_1`, `PV2_3` and `PV2_5` WCS keywords as defined in Greisen and Calabretta (2002)). For the WFC the correction is at the level of 2% in the outer parts of the frames.

It is straightforward to show that an aperture of radius $\approx$FWHM delivers optimal (i.e. 90 per cent of the total flux) photometry compared to more detailed PSF fitting (Naylor 1998) in non crowded areas. After adding some extra refinements to deal with the most crowded regions we find that there is little to be gained from PSF fitting (Irwin et al. 2008, in prep).

In order to determine the effect of possible crowding of our images in our detection we use the nearest neighbour probability density distribution (PDF) expected for a random sample which can be written as (Bahcall and Soneira 1981)

$$P_{NN}(\theta) = 2\pi\rho\theta\, e^{-\pi\rho\theta^2} \qquad (2)$$

where ρ is the average density and $\pi\rho\theta^2$ is the number of neighbours in the interval $(0, \pi\theta^2)$. The expected mean nearest neighbour separation can then be calculated as (Scott and Tout 1989)

$$\langle\,\theta\,\rangle = \int_0^\infty \theta\, P_{NN}(\theta)\, d\theta = \frac{1}{2\sqrt{\rho}} \qquad (3)$$

For the space densities typical of our fields we obtain $\langle\,\theta\,\rangle = 8.5$". We can determine the fraction of missed objects due to crowding by calculating the probability that given a source there is another one within the FWHM of the image, plus to probability that there is third one within that limit, and so on. Integrating over all the possibilities we arrive at the following expression (Irwin and Trimble 1984)

$$\rho_{\rm corr} = -\frac{log(1 - 4\pi\rho\,\theta_{FWHM}^2)}{4\pi\,\theta_{FWHM}^2} \qquad (4)$$

where $\rho_{\rm corr}$ is the corrected average density and θ_{FWHM} the FWHM of the images. For our images this ranges from 0.6% to 0.1%, i.e., negligible for most of the studies.

4 MORPHOLOGICAL CLASSIFICATION

The morphological classification is based primarily on the aperture fluxes and the discrete curve-of-growth for each detected object defined by them. Ancilliary information such as object ellipticity derived from intensity-weighted second moments is also used but only as a secondary indicator. The curve-of-growth is a direct measure of the integral of the point spread function (PSF) out to various radii and is independent of magnitude if the data are properly linearised, and if saturated images are excluded. In using this property the classifier further assumes that the effective PSF for stellar objects is constant over each detector,[1] although individual detectors are allowed to have different PSFs since all detectors, pointings and passbands are treated independently. **– Note: Again this is too much and appears elsewhere. –**

In practice, the aperture with radius $r = 1.2$ arcsec is used as a fixed reference and also defines the internal magnitude (flux) scale. The linearity of the system implies that the position of the stellar locus for *any function* of the aperture fluxes is independent of magnitude (at least until images saturate). Therefore marginalising the flux ratios over magnitude yields one-dimensional distributions that can be used to greatly simplify locating the stellar locus using an iteratively clipped median. With the location estimated, the median of the absolute deviation from the median (MAD) provides a robust measure of the scatter about this locus as a function of magnitude, at least until galaxies dominate in number. This process is repeated iteratively for each distribution, using 3-sigma clipping to remove non-stellar outliers, until satisfactory convergence is reached. After convergence the equivalent Gaussian sigma is estimated using $\sigma_{gauss} = 1.48 MAD$ and by this means each of the image shape descriptors (in this case flux ratios or ellipticity) can be renormalised to follow a zero-median, unit variance Gaussian-like $N(0, 1)$ distribution.

These measures are then directly combined to form the final classification statistic. The combination (essentially a unweighted sum of the normalised signed distributions) is designed to preserve information on the "sharpness" of the object profile and is finally renormalised, as a function of magnitude, to produce the equivalent of an overall $N(0, 1)$ classification statistic.

In practice measures derived from real images do not exactly follow Gaussian distributions. However, by combining multiple normalised distributions (with well-defined 1st and 2nd moments), the Central Limit Theorem works in our favour such that the resulting overall statistic is Gaussian-like to a reasonable approximation and hence can be used with due care as the likelihood component of a Bayesian Classification scheme, making optional use of prior knowledge.

Objects lying within 2–3σ of the stellar locus (*i.e.* of zero) are generally flagged as stellar images, those below –3 to –5σ (*i.e.* sharper) as noise-like, and those above 2–3σ (*i.e.* more diffuse) as non-stellar. Although the discrete classification scheme is based on the $N(0, 1)$ measure of stellar appearance it also has several over-rides built in to attempt to make it more reliable. For example, adjustments to the boundaries at the faint-end (to cope with increased rms noise in the statistic) and at the bright-end (to cope with saturation effects) are also made, while the overall image ellipticity provides a further check.

A by-product of the curve-of-growth analysis and the classification is an estimate of the average PSF aperture correction for

---

[1] In practice we find that the effects of the spatial variation of the PSF on the aperture fluxes at the detector level are generally negligible.

each detector for those apertures (up to and including $4r$, which includes typically ~ 99 per cent, or more, of the total stellar flux) used in deriving the classification statistic. Accurate assessment of the aperture correction to place the (stellar) fluxes on a total flux scale is a crucial component of the overall calibration. We find that this method of deriving aperture corrections contributes $\leqslant \pm 1$ per cent to the overall photometry error budget and also provides a useful first order seeing correction for non-stellar sources. Further by-products of the morphological classification process are improved estimates of the seeing and average PSF ellipticity from making better use of well-defined stellar-only sources. These parameters are required for quality control monitoring of telescope performance and "atmospheric" seeing.

5 PHOTOMETRIC CALIBRATION

Calibration of photometric nights is done using series of Landolt standard stars (Landolt 1992) with photometry in the SDSS system with additional stars from Stetson (2000). For each night a zero point and error estimate using the observations of all the standard fields in each filter is derived. The calibration over the whole mosaic has an accuracy of 1-2 per cent. All calibration is by default corrected during pipeline processing for the mean atmospheric extinction at La Palma (0.46 in U, 0.19 in g, 0.09 in r, 0.05 in i and 0.05 in Z per unit airmass).

Next we derive the colour equations between the WFC and SDSS system. Using DR7 we match the position of all point-like objects (as classified in the WFC images) using the nearest neighbour within a radius of 1 arcsec. For each chip we independently fit a transformation as follows:

$$U_{WFC} = u_{SDSS} + A_U + B_U(u_{SDSS} - g_{SDSS})$$
$$g_{WFC} = g_{SDSS} + A_g + B_g(g_{SDSS} - r_{SDSS})$$
$$r_{WFC} = r_{SDSS} + A_r + B_r(g_{SDSS} - r_{SDSS})$$
$$i_{WFC} = i_{SDSS} + A_i + B_i(r_{SDSS} - i_{SDSS})$$
$$Z_{WFC} = z_{SDSS} + A_Z + B_Z(i_{SDSS} - z_{SDSS})$$

where A_x is the offset between both systems which corresponds to the difference between the Vega and AB systems for the particular band and B_x the colour term. We use PSF magnitudes (corrected using the UberCal calibration) for SDSS and aperture corrected magnitudes with an aperture size selected to match the seeing of the image for the WFC. The difference between the fits for different chips is negligible in the final photometry ($\sim 0.1\%$) so we decided to use one set of equations for all chips. The results in each band are shown in figure 7 and are given by the following equations:

$$U_{WFC} = u_{SDSS} - 0.813 - 0.011\,(u_{SDSS} - g_{SDSS})$$
$$g_{WFC} = g_{SDSS} + 0.106 - 0.135\,(g_{SDSS} - r_{SDSS})$$
$$r_{WFC} = r_{SDSS} - 0.085 + 0.007\,(g_{SDSS} - r_{SDSS})$$
$$i_{WFC} = i_{SDSS} - 0.317 - 0.070\,(r_{SDSS} - i_{SDSS})$$
$$Z_{WFC} = z_{SDSS} - 0.450 - 0.028\,(i_{SDSS} - z_{SDSS})$$

were A_x and B_x and been derived by averaging the values obtained from the fits in each chip.

We use these transformations to derive a zero point for each image but we do not take into account the independent term A_x so the WFC magnitudes are given in the AB system. Figure 8 shows
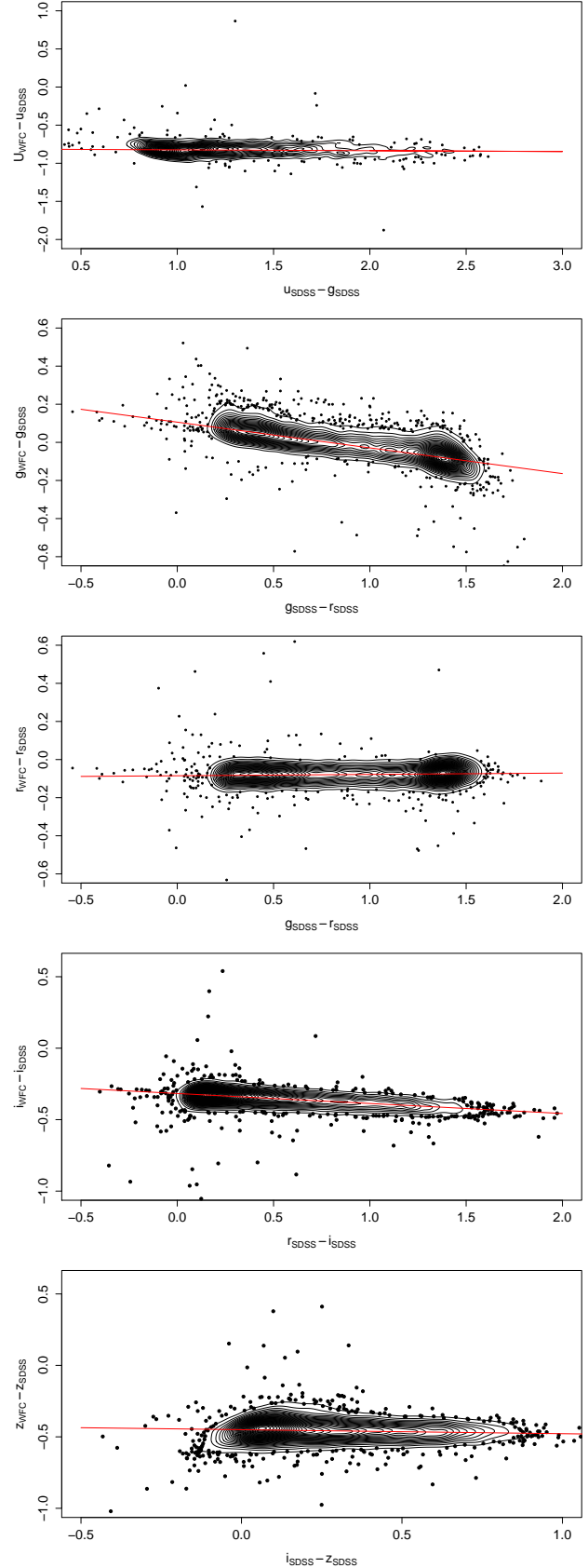

Figure 7. WFC vs SDSS colours and fits used to derive the photometric transformations between both systems. Object density is plotted as contours.

Table 2. Total number detected in each field and percentage of objects detected in each band.

Field	No of objects	U_{WFC}	g_{WFC}	r_{WFC}	i_{WFC}	z_{WFC}
FLS	643699	8%	55%	40%	66%	24%

the derived zero point for each image. The derived values can be used to monitor the photometric quality of data for each particular observation. Zero points are used to derive magnitudes for each source in the following way:

$$m = \text{ZP} + m_{inst} - \kappa(1 - X) - a - 2.5 \log 10(d)$$

where $m_{inst} = -2.5 \log 10(\text{counts}/\text{exptime})$ is the instrumental magnitude, κ is the extinction coefficient, X the airmass, a the aperture correction and d is the distortion correction.

6   BAND MERGE AND CATALOGUE CREATION

All image catalogues are first merged into a single catalogue per band. Duplicate sources arising from overlaps and areas observed more than twice are dealt with by selecting objects within 0.5 arcsec distance of each other and keeping only one of them, selecting the best one based on the signal-to-noise ratio and proximity to any of the chip edges.

A band merged catalogue is then produced by cross matching the different bands within a search radius of 1.2 arcsec and keeping the nearest match. This is done using a kd-tree data structure which allows for fast cross matching between large tables using multiple processors. **– Note: Not sure if it makes sense to go too technical here – only that doing a cross match of several million objects is not so trivial. –**

7   CATALOGUE CONTENTS

The catalogue is divided in two tables, one containing the image derived parameters extracted from the images and another one containing data quality control values, observation parameters and aperture corrections. The contents of the catalogue is summarised in tables 3 and 4.

Aperture corrected magnitudes are given in 13 different aperture sizes, with the minimum being 0.6 arcsec and the maximum being 15.6 arcsec. This defines the curve of growth which can be used to derive the aperture magnitude for any aperture size between these two by interpolation. Note that in order to do this one needs the aperture corrections used which are also provided in the quality control catalogue for apertures 1 to 7 since for larger apertures the correction is null.

Figure 10 shows a colour colour diagram for point-like objects detected in FLS. Figure 11 shows a comparison between SDSS and WFC magnitudes demonstrating their good agreement.

Additionally to aperture corrected magnitude the catalogue software also provides quantities which may be more appropriate for extended objects. These include Petrosian (Yasuda et al. 2001), Kron (Bertin and Arnouts 1996) and Hall (Hall and Mackay 1984) magnitudes and radius.

For each band we also provide one individual star/galaxy classification flag (*?class*) which takes a discrete value as described in
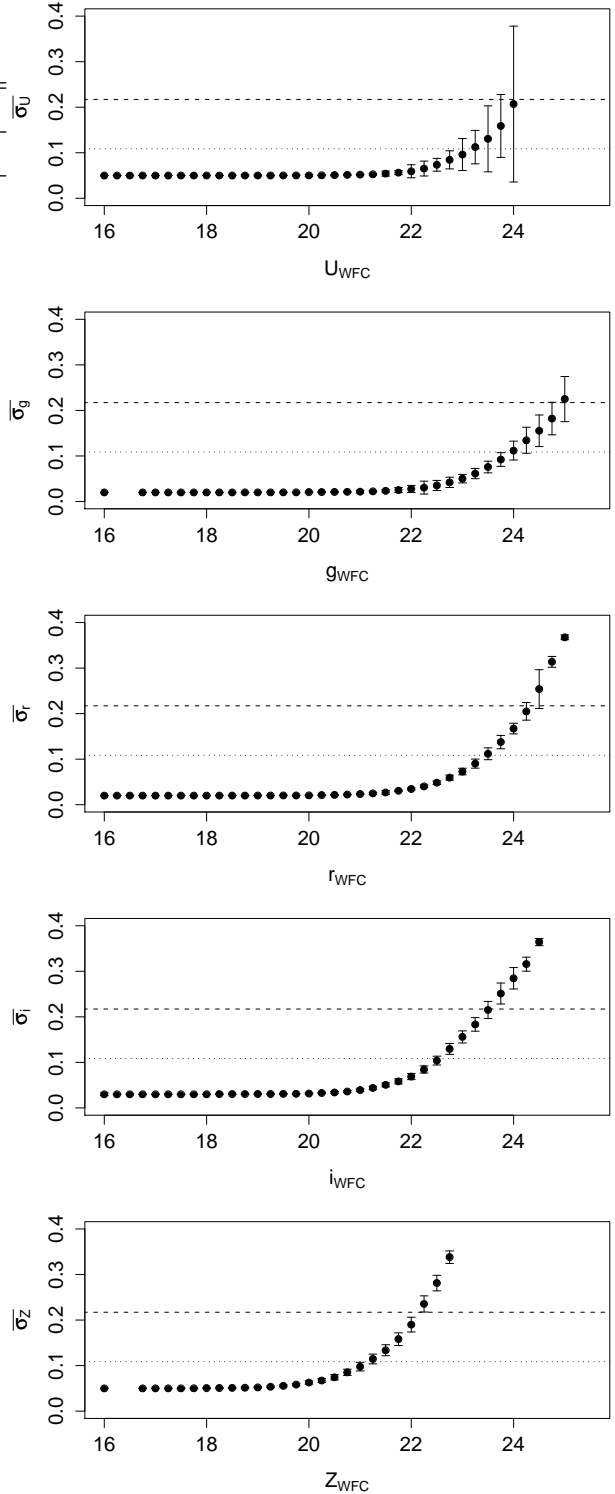

Figure 9. Average magnitude measurement uncertainties in 0.25 mag bins as a function of magnitude. The vertical error bars show the *rms* dispersion in the mean uncertainties in each bin and the horizontal lines show the 5σ (dashed) and 10σ (dotted) levels.
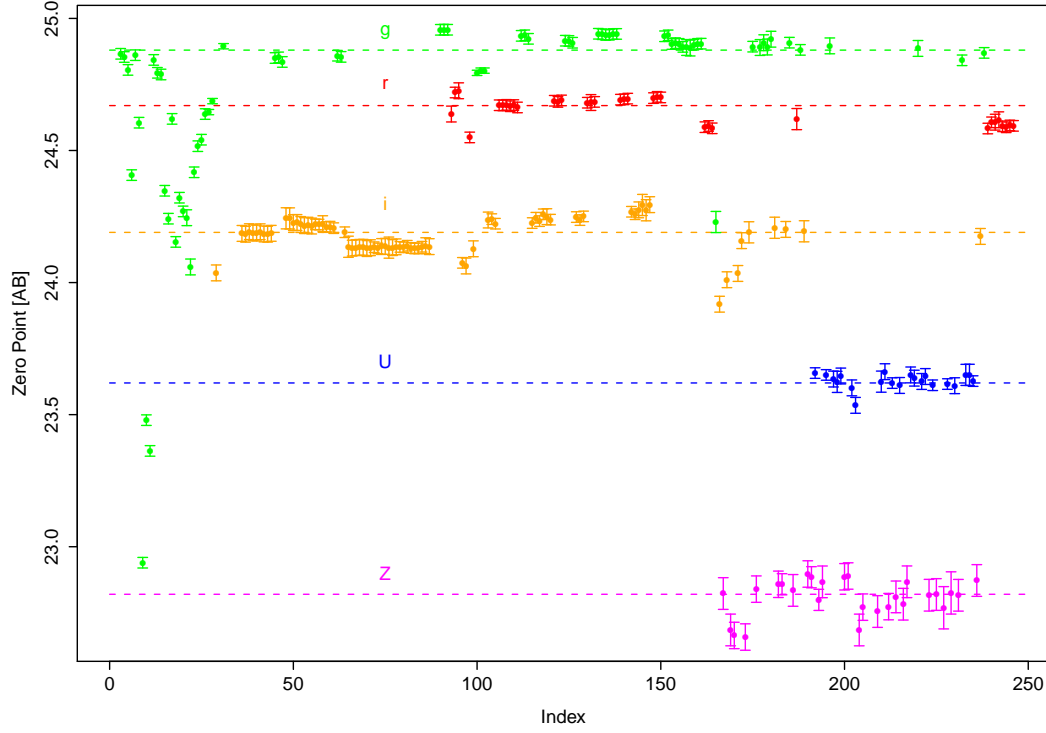
Figure 8. Magnitude zero point of each image of the FLS observations. The dashed line is the median of the zero point for each band.

Table 3. Optical catalogue contents.

Name	Description	Units
id	Object ID	
ra	RA (J2000)	deg
decl	Dec (J2000)	deg
coords	Coordinates in sexagesimal format	
	...begin for each band in order rgiZU...	
rid	Object ID of r band detection	
rmag[1-13]	r band aperture corrected magnitude	AB
remag[1-13]	r band magnitude error	AB
rkronmag	r Kron magnitude	AB
rekronmag	r Kron magnitude error	AB
rkronrad	r Kron radius	arcsec
rhallmag	r Hall magnitude	AB
rehallmag	r Hall magnitude error	AB
rhallrad	r Hall radius	arcsec
rpetromag	r Petrosian magnitude	AB
repetromag	r Petrosian magnitude error	AB
rpetrorad	r Petrosian radius	arcsec
risomag	r Isophotal magnitude	AB
reisomag	r Isophotal magnitude error	AB
rclass	r band star/galaxy classification	
rgauss	r gaussian sigma of source profile	arcsec
rellip	r ellipticity of source	
rflag	mag limit if source not detected, 0 otherwise	
rimage_id	id of image in the QC table	
	...end for each band...	
pstar	combined multiband star class	
pgalaxy	combined multiband galaxy class	
sdss_id	SDSS DR7 catalogue objID of matched source	

Table 4. Optical quality control catalogue contents.

Name	Description	Units
id	Image ID	
runno	Run number of observation	
ccdno	CCD number	
waveband	Band of observation	
instrument	Instrument	
mjd	MJD of observation	
dateobs	Date of observation	
exptime	Exposure time	
apcor[1-7]	aperture correction	AB
avseeing	average seeing of observation	arcsec
avelliptic	average ellipticity of observation	
airmass	airmass of observation	
maglim	magnitude limit of observation	AB
magzpt	magnitude zero point of observation	AB
magzrr	zero point error	AB
skynoise	sky noise	counts
threshold	detection threshold	counts
stdcrms	rms of astrometric fit	arcsec
numbrms	number of stars used in astrometric fit	
wcs	wcs information (multiple keywords)	

table 5. All the individual flags are combined into a merged probability of the object been point-like or extended (*pstar* and *pgalaxy*) using Bayesian classification rules assuming each value is independent:
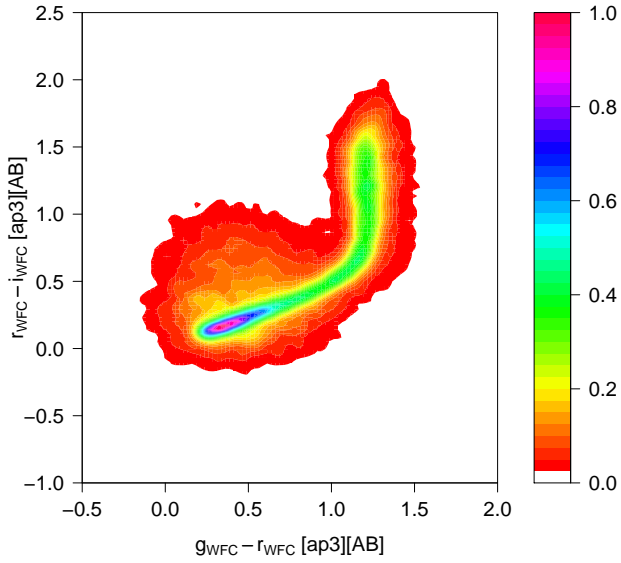
Figure 10. Colour colour plot of all point-like objects detected in FLS. Different colours represent normalised densities according to the colour legend at the right. Note that no faint magnitude cut has been applied.
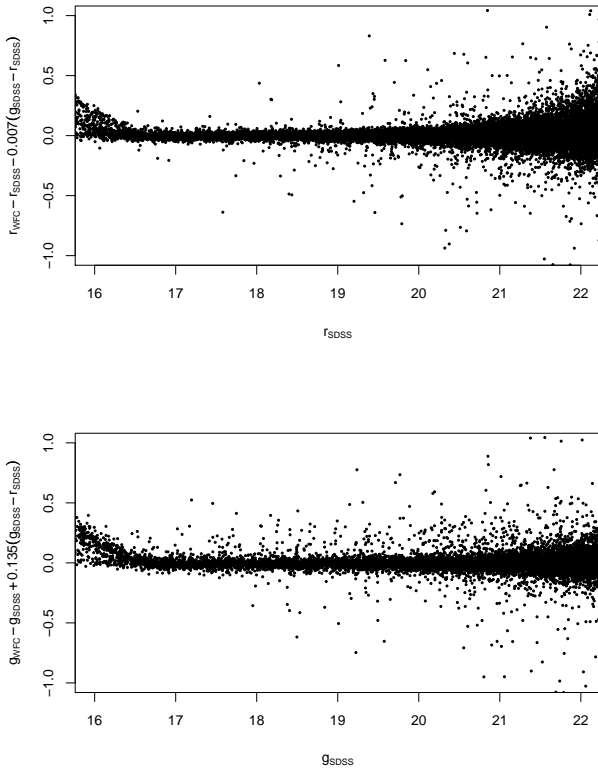

Figure 11. Comparison of SDSS and WFC r and g band magnitudes for point like objects in the FLS.

Index	Meaning	Probability (%)			
		Star	Extended	Noise	Saturated
-9	Saturated	0	0	5	95
-3	Probable extended	25	70	5	0
-2	Probable star	70	25	5	0
-1	Star	90	5	5	0
0	Noise	5	5	90	0
1	Extended	5	90	5	0

Table 5. Meaning of classification index and probability assigned to each of them.

$$P(c_k) = \prod_j P(c_k)_j / \sum_k \prod_j P(c_k)_j \qquad (5)$$

where c_k is the classification flag and i denotes the ith single detection passband measurement available. Decision thresholds for the resulting discrete classification flag are 90 per cent for definitive and 70 per cent for probable. When any of the individual classification flags denote saturation the probability is assigned a value of 255.

Quality control parameters include the average seeing, average ellipticity, magnitude limit, magnitude zero point and its error of the observation in which that particular object has been detected.

Objects for which there is no magnitude available lie in two categories. Either the objects was not detected or the object was not observed. The *?flag* parameters takes the value of the magnitude limit on the former case and zero in the latter.

8   ADDITIONAL DATA

8.1   CFHT U band in FLS

Images obtained in the U band in FLS using the CFHT have been extracted from the archive. These are described elsewhere (ref here). The images from the archive consist in processed individual exposures. We first trim the individual detector images to remove the overscan regions. Then we remove large scale backgrounds using a median filter. After this the images are astrometrically recalibrated using 2MASS sources and a zenithal polynomial astrometric distortion characterised by terms $PV2_1 = 1$, $PV2_3 = 75$ and $PV2_5 = 25000$. Figure 6 shows the effect of this term in the photometry. For MegaCam the correction is at the level of 4% in the outer parts of the frames.

The individual exposures are stacked and mosaicked into one single image per pointing and extracted sources from them using the same software used in the processing of the INT WFC images. Photometric calibration is done using SDSS sources and the following colour equation

$$U_{CFHT} = u_{SDSS} - 0.219 \, (u_{SDSS} - g_{SDSS}) \qquad (6)$$

which differs from the colour term given in (ref here) by ~ 0.02 mag. Aperture magnitudes have been measured with the same aperture radius. The final catalogue after removal of duplicate sources due to pointing overlaps is given as one single table with the pointers to the matched object in the INT/WFC catalogue.

REFERENCES

Bahcall J.N., Soneira R.M., 1981, ApJ, 246, 122

Bertin E., Arnouts S., 1996, , 117, 393

Greisen E.W., Calabretta M.R., 2002, A&A, 395, 1061

Hall P., Mackay C.D., 1984, MNRAS, 210, 979

Irwin M., Lewis J., 2001, New Astronomy Review, 45, 105

Irwin M., McMahon R., Walton N., González-Solares E., Hodgkin S., Irwin J., et al., 2005, The Newsletter of the Isaac Newton Group of Telescopes (ING Newsl.), issue no. 9, p. 8-11., 9, 8

Irwin M.J., 1985, MNRAS, 214, 575

Irwin M.J., Trimble V., 1984, AJ, 89, 83

Landolt A.U., 1992, AJ, 104, 340

McMahon R.G., Walton N.A., Irwin M.J., Lewis J.R., Bunclark P.S., Jones D.H., 2001, New Astronomy Review, 45, 97

Naylor T., 1998, MNRAS, 296, 339

Scott D., Tout C.A., 1989, MNRAS, 241, 109

Stetson P.B., 2000, PASP, 112, 925

Yasuda N., Fukugita M., Narayanan V.K., Lupton R.H., Strateva I., Strauss M.A., et al., 2001, AJ, 122, 1104